Bulletin of the Seismological Society of America, Vol. 94, No. 4, pp. 1492–1499, August 2004

Crustal Scattering and Some Artifacts in Receiver Function Images

by Igor B. Morozov

Abstract The existing 2D and 3D depth imaging approaches using multichannel teleseismic receiver functions (RFs) can result in significant artifacts caused by misinterpretation of signal-generated noise resulting from broadside scattering within the crust. A synthetic example using acquisition geometry of the 1993 Cascadia experiment shows that scattering of the primary *P*-wave arrivals from a sedimentary accretionary wedge could produce RF events close to those observed in real data. Quasi-linear crustal structures with significant velocity contrasts near Moho depths, such as subduction zones, should create particularly strong and coherent noise arrivals. Conventional interpretations of these arrivals based on assumptions of their origin in mode conversions could lead to images of spurious dipping structures of landward dips steeper than ~10° that may be very difficult to distinguish from the true structures. Detailed analysis of prestack, premigration RF data is required for correct identification of the signal-generated noise and validation of the resulting depth images. Identification of scattered events in RF records could also help constrain major crustal structures, such as crustal sutures and subduction fault zones, and particularly those with strong Moho expressions.

Introduction

Teleseismic receiver functions (RFs) have become an accepted standard for imaging the Moho and upper mantle discontinuities, and they are viewed as the primary source of detailed information on the *S*-wave velocity contrasts within the upper mantle (e.g., Shearer, 1991; Bostock, 1998; Dueker and Sheehan, 1998; Shen *et al.*, 1998; Chevrot *et al.*, 1999; Gurrola and Minster, 2000; Rondenay *et al.*, 2001). However, with increasing sophistication of imaging techniques, a tendency for disregarding some of the key specifics of RF data sets, such as their inherently limited apertures and spatial sampling and, in particular, the difficulty of controlling the source-generated noise, still remains and may even have increased.

Due to their reliance on waveform inversion of long codas of *P*-wave arrivals, RF interpretations may be sensitive to contamination of the coda by receiver-end crustal scattering, particularly at frequencies above ~0.5 Hz at which crustal scattering becomes significant (e.g., Bannister *et al.*, 1990; Gupta *et al.*, 1990; Wagner and Langston, 1992; Clouser and Langston, 1995; Abers, 1998; Revenaugh, 2000). Numerous subhorizontally propagating crustal– and upper-mantle–guided phases (*Rg*, *Pg*, *Sg*, *Lg*, *Pn*, and *Sn* plus near-critical crustal and mantle reflections) generated by the primary *P* wave provide a background of signal-generated noise that could be difficult to distinguish from mode conversions in the final images. Similarly to the well-known problem in shallow reflection seismics (e.g., Steeples and Miller, 1998), direct and guided waves may survive stacking and result in spurious images indistinguishable from real geological structures.

Teleseismic recording in the vicinity of a continental boundary could yield examples of coherent scattered noise produced by a strong crustal-scale velocity discontinuity. The vicinity of the trench, combined with the oceanic plate projecting into the mantle, contains by far the strongest crustal-scale horizontal velocity contrasts down to the Earth's core. Due to its alignment along the plate boundary, the trench should cause efficient scattering in the inland direction. Because broadband arrays targeting subducting plates are also typically deployed orthogonally to the continental plate edges, coherent, dipping scattered events should be expected in the resulting depth images. In this article, I use a simplified modeling to illustrate what coherent-noise RF patterns are likely to be observed in such an environment.

The resulting noise synthetics exhibit strong similarities to RF events that are observed in some recent experiments and interpreted as images of the subducting oceanic crust. The scattered noise occupies exactly the same space-time interval as converted waves from the subducting oceanic crust, contains similar frequencies and the same range of linear time-distance moveouts, and is comparable to them in amplitude. Prestack depth migration of the scattered noise records (based on the usual assumptions of mantle mode conversions) leads to a series of spurious landward-dipping structures that could be confused with the subducting lith-

osphere. Therefore, interpretations of such images could become erroneous if broadside scattering noise is not properly isolated.

Receiver-Side Signal-Generated Noise in RF Sections

To illustrate the effects of the source-induced noise in depth RF images, consider scattering recorded by a linear, 50-station array with 5-km spacing between stations and oriented orthogonally to an accretionary wedge starting at 100 km from it (Fig. 1). As the use of 3D simulations does not seem to be justified given the incomplete knowledge of the geometry of the subducting plate and the illustrative character of this study, modeling is performed in a heuristic fashion. To simulate trench scattering, I assume a single scattering depth level and use unperturbed Green's functions for the scattered field computed in the 1D International Association of Seismology and Physics of the Earth's Interior (IASP91) model (Kennett and Engdahl, 1991). I also ignore the difference between the thicknesses of the oceanic and continental crust and use these 1D synthetics simply to produce a representative set of subhorizontally propagating elastic-wave modes. The resulting synthetics thus illustrate the kinematic and the general amplitude character of the scattered field, but they are far from reproducing RF waveforms from any particular experiment.

Three-component synthetic RFs are computed as follows. First, a synthetic Green's function is modeled for a point source in the IASP91 model using the 1D reflectivity method (Fuchs and Müller, 1971). A single bandlimited spike is chosen as the source wavelet, and frequencies between 0.06 and 1.2 Hz are used for modeling. Two end-member examples of Green's functions for shallow and deep scattering are shown in Figure 2; in reality, a complex mixture of similar wave fields originating from all depths would propagate along the array. Note that all such scattered fields would still consist of fans of arrivals diverging from near-crustal levels.

Based on the assumption that the scattering area (point A in Fig. 1) is associated with the subducting oceanic crust, its horizontal position depends on the choice of the scattering depth. The depth to the top of the oceanic crust varies from ~0 km at 100 km offshore to 20–30 km beneath the westernmost station of the array, and therefore the zone of dominant scattering could be located practically anywhere within ~0–100 km from the array. This zone of scattering could also extend inland due to the strong and coherent surface, and apparently Moho, topography of volcanic arcs associated with the subduction. Among other factors, the scattered wave field depends strongly on the depth of its source (Fig. 2).

For shallow scattering (e.g., from the coastline or topography) the wave field should be dominated by the crustal S (L_g) and P waves (Fig. 2, left), whereas for a source near the base of the crust (35 km in the IASP91 model) the direct P and S waves are predominant (Fig. 2, right). This second

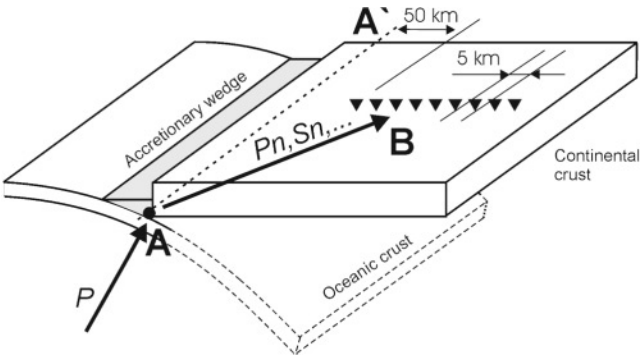

Figure 1. Simplified model of trench-zone scattering. Plane teleseismic wave impinges on the trench area at point A, and scattered waves are recorded at the recording stations, denoted B (triangles). In order to simulate scattering from the trench, point-source scattered field (Fig. 2) is numerically integrated along the line AA′. The subducting oceanic crust (dashed contours) is shown for reference only and is not included in the model.

case could be most relevant for teleseismic waves impinging on the crust from below, and thus we place the scattering area at a depth of 35 km and at 50 km from the array (Fig. 1). This choice also leads to the best match of the synthetics with the 1993 Cascadia 3 observations (see the Discussion).

In order to approximate the linear character of the scattering region (trench AA′, shaded in Fig. 1), the resulting synthetic wave field (Fig. 2, right) was integrated over the length of the wedge:

$$\mathbf{U}(t,\vec{\boldsymbol{r}}) = U_{\mathrm{P}} \int_{-\infty}^{\infty} \Omega(y_{\mathrm{A}})\mathbf{R}_{\mathrm{A-B}} \{\mathbf{G}[t - t_{\mathrm{A}}(y_{\mathrm{A}}), |\vec{\boldsymbol{r}}_{\mathrm{B}} - \vec{\boldsymbol{r}}_{\mathrm{A}}|]\} dy_{\mathrm{A}}, \quad (1)$$

where r_{A} and r_{B} are the radius vectors of the scattering and recording points, respectively, y_{A} is the cross-line coordinate of the scattering point (Fig. 1), $t_{\mathrm{A}}(y_{\mathrm{A}})$ is the time of the primary P-wave onset at point A, and U_{P} is its amplitude. $\mathbf{G}$ is the axially symmetric point-source Green's function (approximated by the sections in Fig. 2), and Ω is the scattering amplitude. Operator $\mathbf{R}_{\mathrm{A-B}}$ rotates $\mathbf{G}$ into the plane of AB (Fig. 1), thereby giving the vector Green's function in 3D. The absolute amplitudes cannot be accounted for in this approximation, and therefore we assume for simplicity $U_{\mathrm{P}} = \Omega(y_{\mathrm{A}}) = 1$. For practical purposes, numerical integration in expression (1) was limited to a 200-km-long segment of the trench.

As the primary arrival consists of a single P-wave pulse, deconvolution of the P-wave waveform at point B is reduced to a time shift, and the three-component RF (denoted $\mathbf{Z}$; Langston and Hammer, 2001) at receiver B thus becomes

$$\mathbf{Z}(\tau,\vec{\boldsymbol{r}}_{\mathrm{B}}) = \mathbf{U}(\tau + t_{\mathrm{B}}, \vec{\boldsymbol{r}}), \quad (2)$$

where t_B is the time of the primary *P*-wave onset on geophone B and τ is the RF time lag.

For a single event with a landward-directed ray parameter of 0.05 sec/km along the axis of the array, the simulated inline component of the RFs scattered from the trench (equation 2) is shown in Figure 3. Note that the model contains no velocity boundaries within the mantle and no *P*/*S* conversions or (other than crustal) multiples of the primary arrival, and thus the entire wave field is due to scattering from the trench area. As expected, for scattering points located deep within the accretionary wedge, the RFs are relatively simple, with direct *P* and *S* waves dominating the section (Fig. 3).

This simplified model illustrates the kinematics and the amplitude relationships of the scattered wave field but does not allow pinpointing the depth and horizontal position of the scattering region. Unfortunately, even 3D simulations would not be likely to resolve this uncertainty because the scattering is observed only by means of nearly horizontally propagating waves. Nevertheless, despite this uncertainty, the linearity of RF events (Fig. 3) still constrains the scattering source to near-crustal depths.

The scattered amplitudes are difficult to constrain because this would require 3D numerical simulations in a structure that is not known accurately. However, a rough estimate of this amplitude can be obtained from the 2D Born approximation of the far-field *P*-wave scattering (Sato and Fehler, 1998; Hong and Kennett, 2003 [their equations 24 and 25]):

$$u^{PP} = i\sqrt{\frac{k^3}{8\pi|\mathbf{r}|}}\, e^{-i(\omega t - k|\mathbf{r}| + \pi/4)}\, C_r(\theta)\int \xi e^{ik(z-\mathbf{kr})} dS, \quad (3)$$

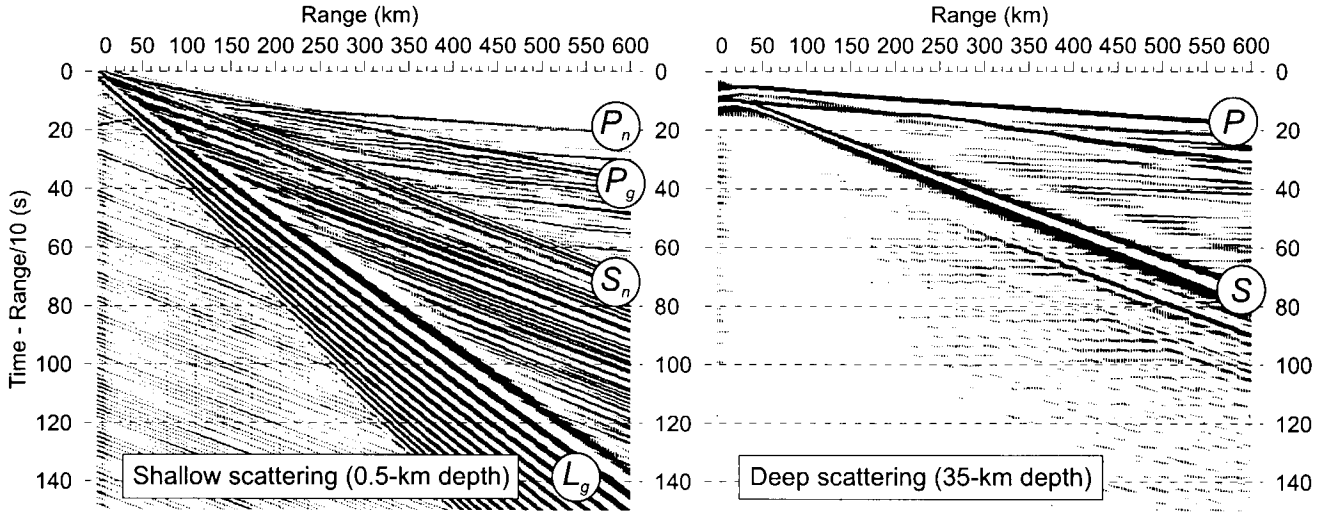

Figure 2. Radial-component wave fields generated by point sources at two depth levels in the 1D IASP91 model using the reflectivity approach (Fuchs and Müller, 1971). Such wave fields approximate the scattered wave field propagating from every point of the accretionary wedge (shown in gray in the inset in Fig. 1). Note the difference between the shallow and deep (near the base of the IASP91 crust) scattering.

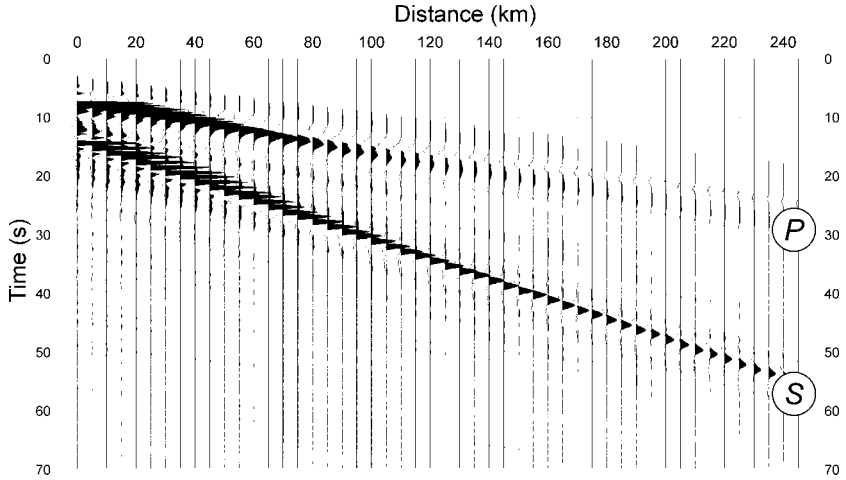

Figure 3. Synthetic inline-component RF for a single event arriving from the left in Figure 1 with ray parameter $p = 0.05$ sec/km.

where **k** is the wave vector in the background medium, **r** is the radius vector from the scatterer to the receiver, t is the time, ω is the angular frequency, θ is the scattering angle, $C_r(\theta)$ is the directional factor equal to 2/3 for $\theta = 90°$, and the integral is taken over the area of the heterogeneity. Equation (3) relates the relative amplitude of the *P*–to–P-wave scattered field, u^{PP}, to the integral of the fractional-fluctuation term $\xi = \delta V_P/V_P = \delta V_S/V_S = \delta\rho/\rho$. Similar relations hold for *P*- to *S*-wave scattering (Sato and Fehler, 1998).

For heterogeneities that are smaller or comparable to the wavelength, we can drop all phase factors in equation (3), resulting in an amplitude estimate for broadside ($\theta = 90°$) scattering:

$$|u^{PP}| = \frac{2}{3}\sqrt{\frac{k^3}{8\pi|\mathbf{r}|}}\,\xi S = \frac{2\pi}{3}\sqrt{\frac{1}{\lambda^3|\mathbf{r}|}}\,\xi S, \qquad (4)$$

where S is the cross-sectional area of the heterogeneity and λ is the wavelength. Substitution of characteristic values of $\lambda = 10$ km, $\xi = 10\%$, and a scattering area of 100 km^2 gives the *P*-wave amplitude of $|u^{PP}| \approx 0.06$ at 100 km from the trench. This amplitude is stronger than the RF amplitudes typically observed (~3% of the primary for the Moho) and drops to 3% only at ~400 km from the trench. Note that the velocity contrasts within the trench area could be stronger than 10% (e.g., crustal against mantle rocks, or sediments against crystalline rocks), and the scattering area larger than in relations (3) and (4). Because of the mantle velocity gradient bending the rays upward, the geometrical spreading would also be slower than $|\mathbf{r}|^{-1/2}$ in formula (4), and there should be pronounced frequency- and polarization-dependent tuning effects due to the proximity of the wavelengths λ to the scale length of the trench area (such as the thickness of the oceanic crust). Consequently, complex fan-like amplitude patterns of trench scattering are likely to dominate RF responses to at least ~400 km from it. Finally, note that the scattering amplitude increases with frequency as $\omega^{3/2}$ (equations 3–4).

Comparison to Field Records

Although not intended as a detailed case study, the model geometry in Figure 2 was chosen to approximate that of the 1993 Cascadia (CASC93) experiment (Nabelek *et al.*, 1993; Trehu *et al.*, 1994) with the purpose of comparing the synthetics to good-quality RF data acquired in an area of active subduction. To date, these data have been analyzed using several RF depth imaging techniques (Nabelek *et al.*, 1993; Rondenay *et al.*, 2001; Bostock, 2002) and have yielded some of the most spectacular images of the subducting oceanic crust. The CASC93 source distribution is shown in Figure 4.

Without questioning the observations of the Cascadian lithospheric slab, let us consider, however, whether the observed CASC93 RF events could be related to scattering

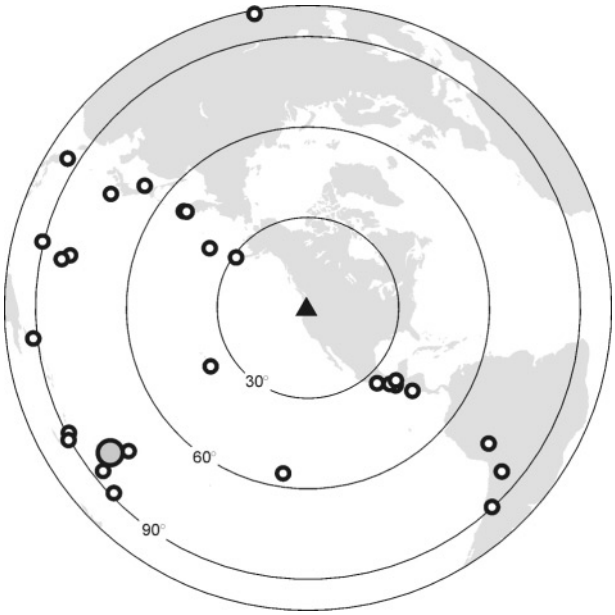

Figure 4. CASC93 source distribution used in Rondenay *et al.* (2001). The event shown with a larger shaded circle is used in Figure 5.

from the trench. Similarly to the synthetics in Figure 2, CASC93 RFs show fans of linear events diverging from a common point near the trench area, with similar moveouts, and visible to ~200 km into the array (figure 3 in Rondenay *et al.* [2001]). The earliest of these arrivals have markedly higher frequencies, as scattered *P* waves would have compared to the *S* waves. The observed RF amplitudes decrease with distance from the trench, also suggesting a source located to the west of the array.

Derivation of RFs is a complex procedure that could complicate mode identification, and a more convincing identification of scattered noise could come from the analysis of the original records. Figure 5 shows a raw vertical-component record section of one of the CASC93 events (Fig. 4). From this record, it is still difficult to unambiguously identify the events contributing to the RFs, and further detailed analysis is required. However, note the abundance of linear events propagating along the array with velocities of ~8.0 km/sec and slower (some are highlighted with dashed lines in Fig. 4), corresponding to *P*- and *S*-wave velocities within the uppermost mantle or within the crust.

Effects on Migrated Images

When interpreted as mode conversions, linear scattered arrivals in time RF images would lead to spurious dipping structure within the depth images. To illustrate this, we perform prestack depth migration of the synthetic RFs under the assumptions of Pp_DS or Pp_DS modes dominating the wave field (converted wave nomenclature from Bostock [1998]). Here and later, migrations are performed using a 3D diffraction-stack algorithm (Morozov and Dueker, 2003b), and

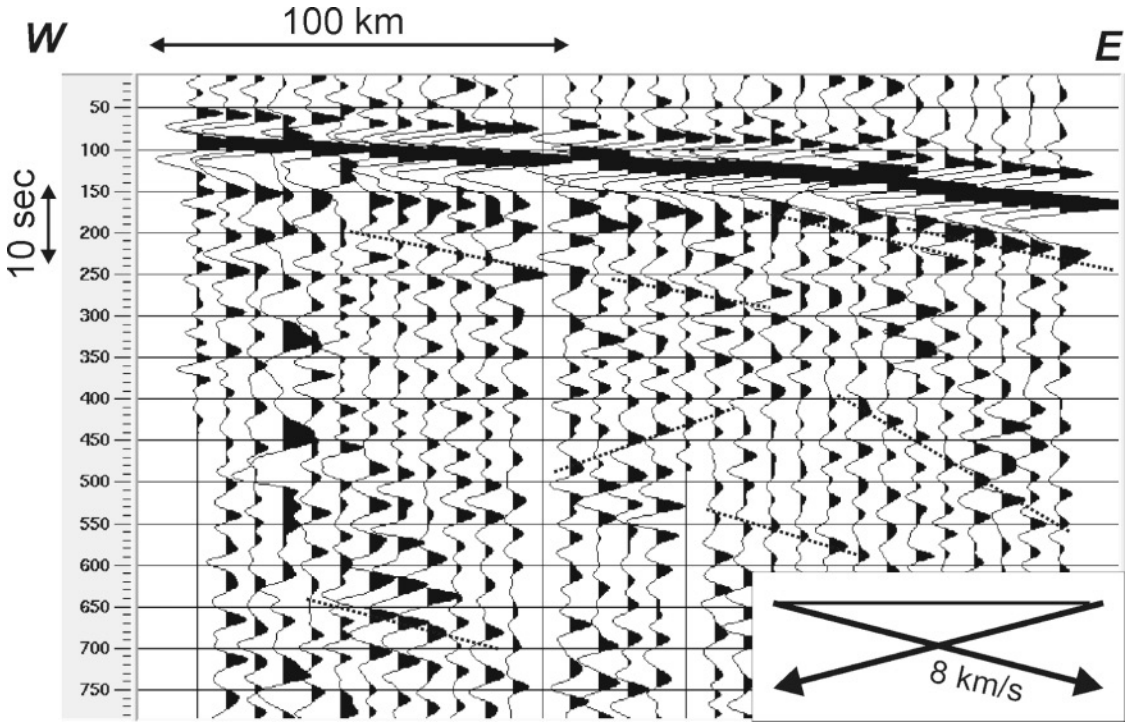

Figure 5. Vertical-component CASC93 records from one event marked in Figure 4, aligned at the onset time of the primary *P* wave on the trench. Note the abundance of energy with crustal and uppermost-mantle moveout velocities in the coda (inset). Some of coherent scattering events are marked with dashed lines. Note that the time axis is annotated in 100-msec increments.

only the axial slices of the resulting image volume are presented. The resulting images (Fig. 6) show spurious linear structures at ~10°, 15°, 28°, and steeper dips, varying thicknesses and polarities, and regions of positive and negative amplitudes that could be confused with high and low S-wave velocity zones. However, these features are merely interference patterns of the aliased lithospheric ground roll. Because of their broad range of dips, such noise wave trains could be very difficult to remove in processing (Steeples and Miller, 1998).

The head-on arrival into the array (from the left in Fig. 1) results in the earliest RF responses, and thus it controls the upper parts of the spurious migrated image. To show that the dipping artifacts do not disappear when multiple events are included, we migrated the synthetics using the CASC93 source distribution (Fig. 4; the event list is from Rondenay *et al.* [2001]). For both modes (Pp_DS and Ps_DS), noise artifacts still resemble dipping *S*-wave velocity contrasts within the mantle. Because of the nonuniform source distribution, these artifacts exhibit yet more complex variations of dips and amplitudes (Fig. 7).

Multimodal imaging (Bostock *et al.*, 2001) enhances RF depth images by combining contributions from several conversion modes (P_DS, Pp_DS, Ps_DS, and others). Unfortunately, these modes are also the most difficult to separate from the broadside scattered noise because they arrive at later times occupied by the slower and more energetic parts of the scattered wave field. Superimposing the backscattered modes also intermixes the scattered wave artifacts and leads to additional interference patterns (Fig. 8). The appearance of such images also depends on the relative weighting of the modes (1:1 in Fig. 8), which is chosen subjectively. Imaging based on the early, P_DS phase would also show artifact events dipping at 15°–35° and starting below ~40 km (Fig. 9; the depth cutoff is due to our use of a deep scattering source).

Discussion and Conclusions

Depth RF imaging utilizes several methodologies from oil-exploration seismics, including moveout corrections, common conversion point stacking (Dueker and Sheehan, 1998; Zhu, 2000), velocity spectrum stacking (Gurrola *et al.*, 1994; Shen *et al.*, 1998), τ-p interpolation (Neal and Pavlis, 1999), and prestack depth migration (e.g., Sheehan *et al.*, 2000; Bostock *et al.*, 2001; Bostock, 2002; Bostock, 2003; Poppeliers and Pavlis, 2003; Morozov and Dueker, 2003b). However, the established reputation of these methods still does not guarantee their immediate success in teleseismic applications. RF imaging differs vastly from its reflection counterpart by its limited apertures, relatively sparse, uneven, and inherently 3D source and receiver distributions,

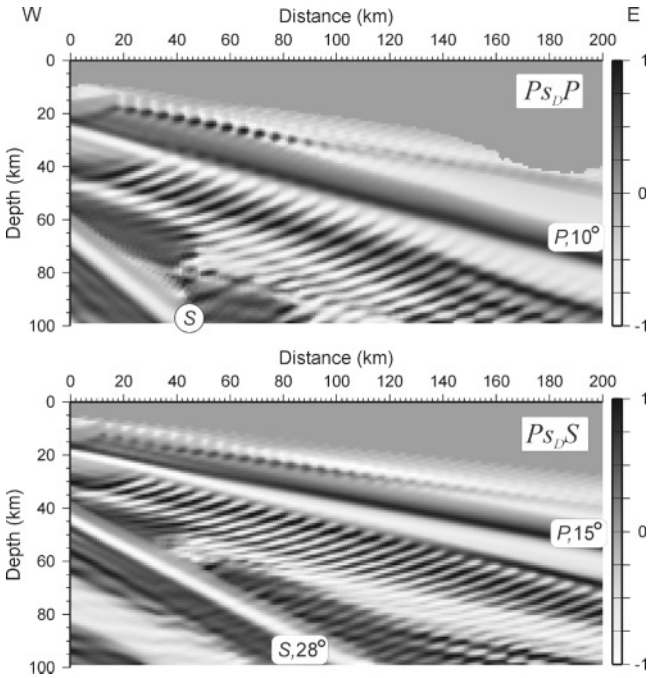

Figure 6. Depth images resulting from prestack depth migration of the event shown in Figure 2 assuming its Pp_DP (top) and Ps_DS (bottom) kinematics. Diffraction-stack migration was performed in 3D (Morozov and Dueker, 2003), and a vertical axial slice of the image is shown; 30° dip filtering was applied to reduce migration smiles due to limited spatial sampling of the receivers. Depth-domain amplitudes are normalized using a 20-km Automatic Gain Control (AGC), with positive amplitudes shown in black and negative in white. Note the dipping artifacts in both images, but at different positions. Labels indicate the apparent dips of the artifact structures.

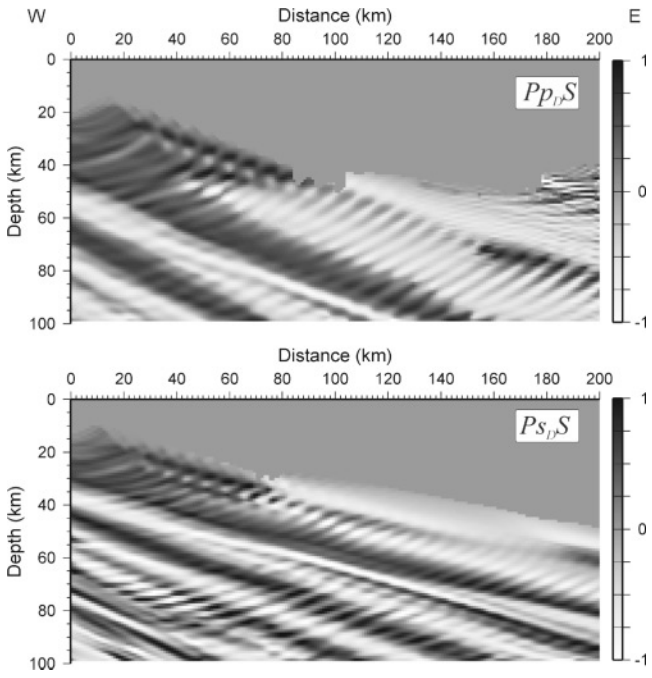

Figure 7. Migration of the synthetic scattering records using the CASC93 source distribution (Fig. 4). Pp_DS (top) and Ps_DS (bottom) mode migrations are shown. Trace presentation as in Figure 6. The coherent noise scattered from the trench area still retains its appearance of a dipping structure in the depth image. Because of uneven source distribution, this noise also acquires variable apparent dips, wavelengths, and amplitudes.

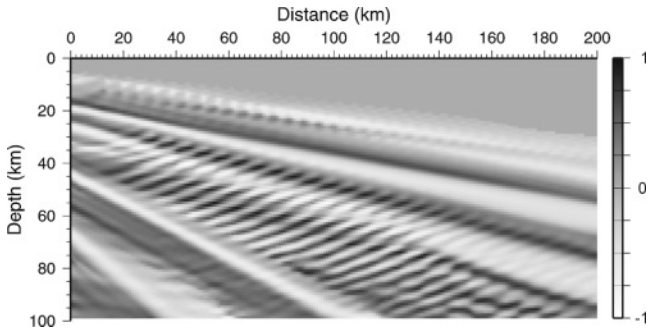

Figure 8. A 1:1 sum of the results of Pp_DS and Ps_DS inversions of synthetic RFs from a single event (Fig. 6). Note that the superposition of these modes changes the image of the coherent noise; nevertheless, its linear and dipping appearance persists. Trace normalization as in Figure 6.

and the necessity to perform deconvolution to extract usable signal from the coda. In consequence, one might expect that reflection imaging methods might require careful scrutiny when applied to RF data.

In the difficulty of its coherent-noise environment, RF imaging appears to be closer to shallow reflection seismics, where strong source-generated noise often overrides useful reflections and potential pitfalls abound (Steeples and Miller, 1998). Identification of the scattered phases requires dense arrays not aliased to the surface waves (cf. Bannister *et al.*, 1990; Gupta *et al.*, 1990; Abers, 1998); however, because of limited resources, this type of deployment is rare in today's RF work. In lieu of unaliased recording, detailed prestack analysis of depth-domain records could help monitor the ways RF images are formed (Morozov and Dueker, 2003a,b).

Note that the dipping artifact structures appearing in migrated RF depth images are not due to a particular type of multichannel processing or a choice of prestack depth migration algorithm. For a single station at kilometer 50 in Figure 6, the scattered phases also resemble conversions from mantle discontinuities dipping away from the trench (Fig. 10). However, unlike array recordings, a single station's RFs do not offer any means (at least kinematic) for distinguishing converted waves on a dipping slab from scattered waves originating at its hinge. Consequently, with single-station recordings, the ambivalence of interpretation is higher.

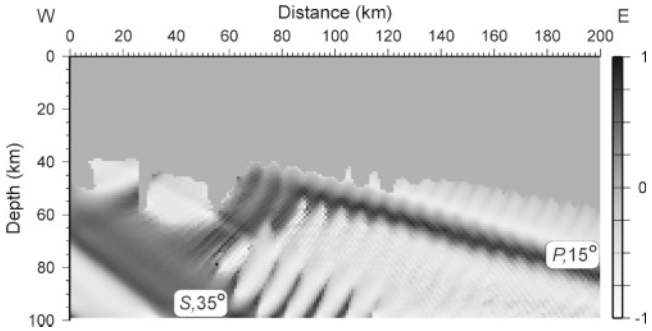

Figure 9. Migration of the same synthetic event as in Figure 6 but assuming a forward *P*-*S* scattering (P_DS) mode kinematics. Note that the image is dominated by steeper dipping events emerging from the trench region. Amplitude presentation as in Figure 6. Labels indicate the primary scattered phases and the dips of the resulting apparent structures.

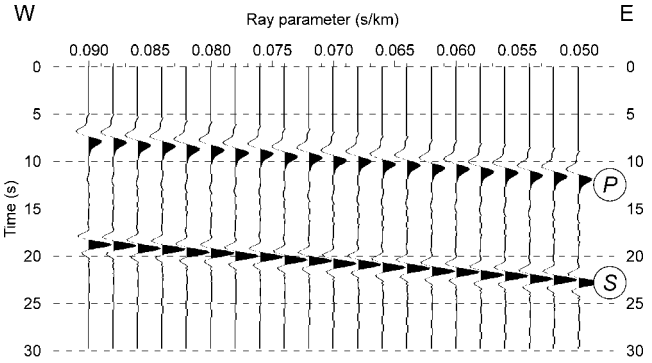

Figure 10. Synthetic RFs representing scattering of multiple events from varying distances and recorded at a single station at 50 km from the front of our array (Fig. 1). When sorted by decreasing ray parameters (corresponding to the increasing epicenral distance), the horizontal coordinate is related to the horizontal position of the ray-theoretical P_DS conversion point (cf. Bostock, 1998), and the image could be interpreted as representing two dipping discontinuities. Note that similarly to Figure 6, these spurious discontinuities project back to the trench.

In prestack, pre-RF teleseismic records, broadside-scattered waves could potentially be distinguished from mode conversions by their independence from the backazimuths and amplitude decays. In the case of a subducting plate discussed here, scattered phases exhibit geometrical spreading and decrease in amplitude away from the trench, whereas mode conversions should show no decay unless the *S*-wave velocity contrast between the subducting oceanic crust and the host mantle is assumed quickly decreasing with depth. Measurements of the amplitude decay would require dense sampling and true-amplitude processing prior to RF generation.

Another criterion that could potentially discriminate between the trench-scattered and boundary-converted waves could be the frequency variations of the observed energy with distance. Because of the effect of seismic attenuation, higher-frequency scattered waves should be observed at closer distances from the trench. Again, qualitatively, this prediction seems to be supported by the observations of a shorter image in the higher-frequency Kirchhoff inversion of the CASC93 data (Bostock, 2002).

The example of an accretionary wedge given earlier highlighted just one potential problem of underestimating crustal scattering in high-resolution (i.e., shorter-period) RF imaging. I used the example of an array targeting subducting oceanic lithosphere because of its relative simplicity and the availability of an excellent CASC93 RF data display (Rondenay *et al.*, 2001) for comparison. However, arrays deployed away from plate boundaries are also likely to record scattering caused by Moho relief, rugged topography, coastlines, sedimentary basins, and crustal faults (Abers, 1998; Revenaugh, 2000). Crustal-scale fault zones projecting into the mantle, such as those observed in lithoprobe reflection studies (Cook *et al.*, 1997) and associated with shallow and oblique lithospheric subduction (Bostock, 1998), could represent intracontinental sources of strong scattering similar to the one discussed here.

The principal conclusion of this study is cautionary: it appears that RF interpretations, including those using multichannel recordings and prestack, multimodal depth imaging, may be subject to a danger of misinterpretation from underestimated receiver-end crustal scattering. In particular, where a linear structure is found dipping steeper than $\sim 10°$, its alternative interpretation as resulting from scattered waves originating at the hinge of that structure should be considered. Apparently the only way to alleviate this ambiguity is to analyze and isolate the coherently scattered noise, preferably before converting the records into RFs. Overall, the reliability of higher-frequency multichannel teleseismic results would benefit from stronger emphasis on presentation and analysis of the data records as compared to models and inversion algorithms. Recognition of the scattered noise in teleseismic records could not only help avoid unbalanced interpretations, but also help identify major crustal structures, particularly those with strong horizontal velocity contrasts at depth, such as crustal sutures, subduction fault zones, and mountain belt roots.

Acknowledgments

This research was supported in part by Defense Threat Reduction Agency Grants DTRA01-01-C-0057 and DTRA01-01-C-0081. CASC93 data were made available through the IRIS Data Management Center. I thank Ken Dueker for his discussions during the initial stage of this work.

References

Abers, G. A. (1998). Array measurements of phase used in receiver function calculations: importance of scattering, *Bull. Seism. Soc. Am.* **88,** 313–318.

Bannister, S. G., E. S. Husebye, and B. O. Ruud (1990). Teleseismic *P* coda analyzed by three-component and array techniques: determin-

istic location of topographic *P*-to-*Rg* scattering near the NORESS array, *Bull. Seism. Soc. Am.* **80,** 1969–1986.

Bostock, M. G. (1998). Mantle stratigraphy and evolution of the Slave province, *J. Geophys. Res.* **103,** 21,183–21,200.

Bostock, M. G. (2002). Kirchhoff-approximate inversion of teleseismic wavefields, *Geophys. J. Int.* **149,** 787–795.

Bostock, M. G. (2003). Linearized inverse scattering of teleseismic waves for anisotropic crust and mantle structure—I. Theory, *J. Geophys. Res.* **108,** 2258, doi 10.1029/2002JB001950.

Bostock, M. G., S. Rondenay, and L. Shragge (2001). Multi-parameter 2-D inversion of scattered teleseismic body waves—I. Theory for oblique incidence, *J. Geophys. Res.* **106,** 30,771–30,782.

Chevrot, S., L. Vinnik, and J. P. Mintagner (1999). Global-scale analysis of the mantle *Ps* phases, *J. Geophys. Res.* **104,** 20,203–20,219.

Clouser, R. H., and C. A. Langston (1995). Modeling observed *P-Rg* conversions from isolated topographic features near the NORESS array, *Bull. Seism. Soc. Am.* **85,** 195–211.

Cook, F. A., A. J. Van der Velden, and K. W. Hall (1997). Upper mantle reflectors beneath the SNORCLE transect: images of the base of the lithosphere? in *Slave-Northern-Cordillera Lithospheric Evolution (SNORCLE) Transect and Cordilleran Tectonics Workshop Meeting*, edited by F. Cook and P. Erdmer, Univ. of Calgary, Alberta, 58–62.

Dueker, K. G., and A. F. Sheehan (1998). Mantle discontinuity structure beneath the Colorado Rocky Mountains and High Plains, *J. Geophys. Res.* **103,** 7153–7169.

Fuchs, K., and G. Müller (1971). Computation of synthetic seismograms with the reflectivity method and comparison with observations, *J. R. Astr. Soc.* **23,** 417–433.

Gupta, I. N., C. S. Lynnes, T. W. McElfresh, and R. A. Wagner (1990). *F–K* analysis of NORESS array and single-station data to identify sources of near-receiver and near-source scattering, *Bull. Seism. Soc. Am.* **80,** 2227–2241.

Gurrola, H., and J. B. Minster (2000). Evidence for local variations in the depth to the 410-km discontinuity beneath Albuquerque, New Mexico, *J. Geophys. Res.* **105,** 10,847–10,856.

Gurrola, H., J. B. Minster, and T. Owens (1994). The use of velocity spectrum for stacking receiver functions and imaging upper mantle discontinuities, *Geophys. J. Int.* **117,** 427–440.

Hong, T.-K., and B. L. N. Kennett (2003). Scattering attenuation of 2D elastic waves: theory and numerical modeling using a wavelet-based method, *Bull. Seism. Soc. Am.* **93,** 922–938.

Kennett, B. L. N., and E. R. Engdahl (1991). Traveltimes for global earthquake location and phase identification, *Geophys. J. Int.* **105,** 429–465.

Langston, C. A., and K. Hammer (2001). The vertical component *P*-wave receiver function, *Bull. Seism. Soc. Am.* **91,** 1805–1819.

Morozov, I. B., and K. G. Dueker (2003a). Signal-to-noise ratios of teleseismic receiver functions and effectiveness of stacking for their enhancement, *J. Geophys. Res.* **108,** 2106 doi 10.1029/2001JB001692.

Morozov, I. B., and K. G. Dueker (2003b). Depth-domain processing of teleseismic receiver functions and generalized three-dimensional imaging, *Bull. Seism. Soc. Am.* **93,** 1984–1993.

Nabelek, J., X.-Q. Li, S. Azevedo, J. Braunmiller, A. Fabritius, B. Leimer, A. M. Tréhu, and G. Zandt (1993). A high-resolution image of the Cascadia subduction zone from teleseismic converted phases recorded by a broad-band seismic array, *EOS* **74** no. 43, (Fall. Meet. Suppl.), 431.

Neal, S. L., and G. L. Pavlis (1999). Imaging *P*-to-*S* conversions with multichannel receiver functions, *Geophys. Res. Lett.* **26,** 2581–2584.

Poppeliers, C., and G. L. Pavlis (2003). Three-dimensional, prestack, plane-wave migration of teleseismic *P*-to-*S* converted phases—I: Theory, *J. Geophys. Res.* **108,** 2112 doi 10.1029/2001JB000216.

Revenaugh, J. (2000). The relation of crustal scattering to seismicity in southern California, *J. Geophys. Res.* **105,** 25,403–25,422.

Rondanay, S., M. G. Bostock, and J. Shragge (2001). Multiparameter two-dimensional inversion of scattered teleseismic body waves—III. Application to the Cascadia 1993 data set, *J. Geophys. Res.* **106,** 30,795–30,807.

Sato, H., and M. Fehler (1998). *Seismic Wave Propagation and Scattering in the Heterogeneous Earth*, Springer, New York.

Shearer, P. M. (1991). Constraints on upper mantle discontinuities from observations of long-period reflected and converted phases, *J. Geophys. Res.* **96,** 18,147–18,182.

Sheehan, A. F., P. Shearer, H. J. Gilbert., and K. G. Dueker (2000). Seismic migration processing of *P-SV* converted phases for mantle discontinuity structure beneath the Snake River Plain, western United States, *J. Geophys. Res.* **105,** 19,055–19,065.

Shen, Y., S. C. Solomon, I. T. Byarnason, and C. J. Wolfe (1998). Seismic evidence for a lower-mantle origin of the Iceland Plume, *Nature* **395,** 62–65.

Steeples, D. W., and R. D. Miller (1998). Avoiding pitfalls in shallow seismic reflection surveys, *Geophysics* **63,** 1213–1224.

Trehu, A. M., I. Asudeh, T. M. Broher, J. H. Luetgert, W. D. Mooney, J. I. Nabelek, and Y. Nakamura (1994). Crustal architecture of the Cascadia Forearc, *Science* **266** 237–243.

Wagner, R. A., and G. A. Langston (1992). Body-to-surface wave scattered energy in teleseismic coda observed at the NORESS seismic array, *Bull. Seism. Soc. Am.* **82,** 2126–2138.

Zhu, L. (2000). Crustal structure across the San Andreas Fault, southern California from teleseismic converted waves, *Earth Planet. Sci. Lett.* **179,** 183–190.

Department of Geological Sciences
University of Saskatchewan
Saskatoon, SK S7N 5E2, Canada
igor.morozov@usask.ca

Manuscript received 10 June 2003.